A comparative study of Light Collector Systems for use with Multi-Anode Photo-Multipliers

Alessandro Petrolini

Dipartimento di Fisica dell'Università di Genova and INFN, Via Dodecaneso 33, I-16146 Genova, Italy.

Abstract

A comparative study of possible Light Collector Systems, designed to increase the geometrical acceptance of commercial Multi-Anode Photo-Multipliers, is presented. A detailed ray tracing study was carried on to evaluate and compare the performance of the different systems, under realistic hypotheses.

Key words: photo-detector, photo-multiplier, light collector, light pipe, lens
PACS:

1 Introduction

Many modern experiments require to cover a large focal surface with photo-sensors capable of single photon detection, position determination with a pixel size of the order of a few mm and a time response of the order of a few tens of ns. In many cases Multi-Anode Photo-Multipliers (MAPMT) represent the most attractive choice [1,2,3,4].

The non-sensitive region usually present at the edge of present MAPMTs, around the central sensitive area, prevents from obtaining a uniform geometrical acceptance on a large surface, when close packing of many devices is required.

Several ideas have been proposed in recent years to overcome this limitation, based on the installation of a suitable Light Collector System (LCS) in front of the MAPMT. The necessity to understand the performance and limits of

Email address: `Alessandro.Petrolini@ge.infn.it` (Alessandro Petrolini).

these systems, for a proper photo-detector design, has motivated the present work. The performance of some possible LCS has been evaluated and different systems were compared by means of a detailed ray tracing simulation.

2 The Hamamatsu R7600 Multi-Anode Photo-Multipliers Tubes

Hamamatsu Corporation produces the R7600 [5] series of MAPMTs, with different pixel size and number. The physical dimension of the MAPMT section is 25.7×25.7 mm^2 and the length is about 30 mm. The tube is equipped with a bialkali photo-cathode and a 0.8 mm thick input window. The availability of different pixel sizes proves to be extremely useful to match the required instrument characteristics.

However the present devices have a low sensitive to total area ratio of about 0.45. The device with the largest number of pixels (R7600-M64) has 8×8 square pixels of 2 mm side and 2.3 mm pitch, giving a maximum sensitive area of about 18.4×18.4 mm^2. All around any pixel there is a low efficiency region about 0.15 mm large. Devices with larger pixel sizes (that is twice and four times) are also available. The R7600-M16 has 4×4 square pixels of 4 mm side and 4.5 mm pitch, giving a maximum sensitive area of about 18.0×18.0 mm^2. All around any pixel there is a low efficiency region about 0.25 mm large. Both versions of the MAPMT have a ratio between the sensitive area and the total area (geometrical acceptance) of about 0.45, assuming an average efficiency in the low efficiency inter-pixel regions equal to one half the maximum efficiency at the center of each pixel. This is a crude estimate, consistent with measurements. One should keep in mind that when packing a number of MAPMTs the real pitch between MAPMTs will be slightly larger than the real MAPMT size (i.e. 25.7 mm), due to engineering constraints, (e.g. the mechanical structure and a possible magnetic and/or electrostatic screen). This reduces even more the overall average geometrical acceptance. Moreover the large mechanical tolerances quoted by the manufacturer (± 0.5 mm) on the dimensions of the device require a correspondingly larger spacing.

An *R&D* program was carried on, in the framework of two different experiments having similar requirements [3,4], to find possible solutions to the problem.

Recently new devices with a better geometrical acceptance have been released (i.e. a weakly focused version of the R7600 MAPMT and the Flat Panel PMT) [6]. While in both cases the ratio between the sensitive area and the total area approaches unity, the packing of different devices would give dead regions in any case. A LCS of the type described in this paper would require a smaller demagnification factor for use with these new devices, which would make the design easier and the performance better compared to the LCS described in the present paper, designed for the classical version of the MAPMT.

3 Possible Light Collector Systems (LCS)

An *R&D* program has been carried on to find possible solutions to the problem of the low overall geometrical acceptance of the MAPMT, which would strongly limit the usefulness of the bare commercial device whenever a uniform acceptance is required on a large surface.

In significant cases, namely when the MAPMTs are used as the light sensors on the focal surface of some primary optical system, the main problem is not the low overall average geometrical acceptance, but the fact that the resulting geometrical acceptance is non-uniform on the focal surface. In fact the focal surface would consist of sensitive regions, at the center of each MAPMT, separated by the totally blind regions, at the edge of each device. This became even worse when one considers the required clearance between the close-packed MAPMTs. The use of LCS, even when it produces only a small increase of the overall average geometrical acceptance, might be nevertheless very useful to make a more uniform geometrical acceptance on the focal surface.

As a design goal the requirement to obtain an overall light collection efficiency larger than the one provided by the bare device (i.e. ≥ 0.5) and with a small dependence on the position will be assumed.

The geometrical acceptance can be improved by means of a suitable LCS, to be placed in front of each device, and performing the required demagnification onto the MAPMT sensitive area. This system might consist of a lens system, a system made of a bundle of tapered light pipes (working either by normal reflection or by total internal reflection inside a transparent medium) or a fiber optic taper.

In this paper the use of the 64-channel MAPMT is assumed, as it provides the maximum pixel density. The use of the 16-channel version would make the design of the LCS even easier due to the bigger pixel size (allowing to accept larger image aberrations) and to the smaller number of channels (requiring a less complex device).

It should be noted that while the LCS has to be an imaging system, due to the multi-pixel structure of the MAPMTs, the optical requirements on its performance are rather poor, as compared to standard optics, because the smallest available MAPMT pixel size is 2 mm.

It is important to stress that the performance of the LCS strongly depends on the angular distribution of the photons at the LCS entrance face. In the present paper a maximum incidence angle (θ_{M}) of the photons up to 25°, will be considered, which would roughly correspond to a main optics with an f-number as low as $f/\# \approx 1.1$.

It must be stressed that the detailed design of any LCS must be optimized for the specific application (i.e. primary optics), it is aimed for. Therefore all the designs discussed in the present paper must be considered only as illustrative examples, without any attempt to perform a real optimization of the design.

3.1 Tapered light pipes system (LP)

The Winston cone [7] has been used since a long time to collect light on photomultiplier tubes. As the Winston cone is a non-imaging system it cannot be used on the MAPMT as a whole. One single tapered light pipe per pixel has to be used, in a multiple Winston cone arrangement. This might exploit either the total internal reflection inside a transparent light pipe or normal reflection on the walls of an empty pipe. The use of this specific kind of LCS would have the advantage to reduce the effect of the low efficiency regions between pixels. Moreover it might help, in principle, to fit a curved focal surface, by suitably shaping the entrance window of the pipes.

The use of tapered light pipes to collect light on a smaller detector (or, to diffuse light from a small source) is well known [8]. The maximum achievable demagnification depends on the angular spread of the incoming rays and on the refractive indexes of the involved materials. Squeezing the cross section of a bundle of photons gives rise to a corresponding increase of the angular divergence of the bundle, setting a limit to the total allowed demagnification [7].

One possibility is to assemble a system made of 8×8 square-section tapered slanted light pipes, one for each pixel, in such a way that each pipe has an exit face with the same dimensions of the MAPMT pixel, and entrance face with dimensions of $(1/8 \times 1/8)$ of the (25.7×25.7) mm^2 corresponding to the physical dimensions of the MAPMT. Actually the dimension of the exit face might be slightly smaller than the MAPMT pixel dimension, to concentrate the photons on the central, more efficient region of the pixel. Similarly the entrance face might be slightly larger than required by the physical MAPMT dimensions to recover the unavoidable clearance due to the MAPMT close-packing and to optimize the packing of the devices on a curved focal surface. In this paper a pitch of 27.0 mm between MAPMTs will be assumed, to be compared to the 25.7 mm size of the MAPMT.

The bundle of tapered light pipes should be arranged in such way that a one to one mapping between 8×8 ideal square pixels on the focal surface and the real 8×8 square pixels of the MAPMT is obtained. Each pipe would have the shape of a truncated skew pyramid with square bases, parallel to each other. Note that, because of symmetry only 16 different shapes of the single pipes are required. Such an arrangement would leave some distance among the neighboring pipes, near the exit face, useful to avoid the ≈ 0.3 mm low efficiency region between the MAPMT pixels. On the other hand the spacing between pipes should be kept at the minimum at the entrance side, to reduce the geometrical inefficiency. In this paper the meaning of *length of the pipes* is the distance between the two parallel planes defining the entrance and exit faces of the pipe, that is the two bases of the pyramid, and not the length measured along the axis (which would depend on the geometry of the specific pipe).

The system based on tapered light pipes has the advantage that the imaging from the focal surface to the photo-cathode is not distorted inside the pixel granularity. Moreover the inefficient regions between pixels are recovered. No additional surface is added (and reflection losses are therefore not worse than with the MAPMT alone) in the case of the system based on normal reflection.

A tapered light pipe system LCS was studied, either in the framework of the AirWatch program [9] and for the LHCb-RICH experiment [10]. This kind of LCS was recently studied also by a Japanese RIKEN group [11].

3.1.1 Total Internal Reflection tapered light pipes system (LP-TIR)

The first possible implementation is by means of solid transparent pipes working by total internal reflection. As the photons are driven to the MAPMT entrance window by total internal reflection, a negligible loss is introduced at each reflection, provided the surface finish is good enough and the photon incidence angles on the walls do not violate the total internal reflection limit. If the system can be assembled leaving the space among the pipes empty then the refractive index outside each pipe would be $\simeq 1$. In case the design of the LCS would require to fill this space, then each pipe would have to be coated with a low refractive index material to ensure, as far as possible, total internal reflection.

The entrance face of the pipes has to coincide with the focal surface of the main optics. It can be coated with an anti-reflection coating to decrease the reflection losses. To minimize reflection losses and avoid total internal reflection at the exit face of the tapered light pipes the latter might be placed in optical contact with the MAPMT input window. As the material composing the light pipe and the one composing the MAPMT input window would have very similar refractive indexes, the reflection losses at the interface would be small. Actually the optical coupling with the MAPMT input window is a critical point of this device. If this cannot be obtained light losses due to total internal reflection at the exit face of the pipe might occur, while the reflection losses might always be reduced by an anti-reflection coating.

If the length of the LCS is too short the rays might reach a point where the total internal reflection condition is violated and the rays will then leak out of the light pipe. In this case not only the photon is lost but, if precautions are not taken, it might show up in another channel creating a cross-talk. If, on the other hand, the length of the pipe is too long the absorption inside the pipe might become unacceptable, as well as its mass and dimensions. The length of the system is therefore one of the parameters which need to be optimized. The performance of the external light pipes, the most critical ones, as they have to produce the largest change in direction of the incident photons, might be improved by giving a suitable tilt to the entrance face.

The tracing of a few rays inside a LP-TIR, is shown, for illustrative purposes, in figure 1.

3.1.1.1 Realization issues. The main requirement is not the mechanical precision, because the system is inherently stable for small variations from design values as long as one stays away from the critical conditions when rays start to be lost on the lateral walls because the total internal reflection condition is violated. The main requirements will be on the smoothness of the walls, to reduce imperfections that would cause ray losses, and on the good optical coupling with the MAPMT entrance window.

One possibility is to assemble the 64 pipes by cementing on the entrance and exit face of the pipes a thin sheet of the same material the pipes are composed of. The sheet on the entrance face would slightly degrade the performance of the system, by making the space resolution slightly worse, because the first refraction would take place slightly before the light pipe starts possibly producing some amount of cross-talk. The sheet on the exit face would produce some light loss because photons exiting from the pipe would have a larger probability to fall inside the inter-pixel low efficiency region.

Depending on the operating wavelength the use of plastics (e.g. PMMA) for the LP-TIR might be a good choice. It could be made also in quartz (see section 5), but in this case it might turn out to be quite expensive [12]. A cheaper possibility is provided by the use of the Sol-Gel technology (see section 5). Except for the use of plastics, mass might be an issue for some applications.

The AMS experiment has recently implemented a similar LCS [13] for the 16-channel version of the MAPMT.

3.1.2 Reflecting tapered light pipes system (LP-R)

The same geometry discussed for the total internal reflection tapered light pipe system might be used for a system exploiting normal reflection on the walls of a bundle of empty pipes. This kind of system would have the advantage of no bulk absorption and no limits due to total internal reflection requirement. However the number of reflection required, the fact that the reflection coefficient is normally dependent on the incidence angle, the large range of the angles of incidence of the photons on the reflecting walls and the requirement of a very good reflectivity impose strict constraints on the coating of the walls to avoid unacceptable light losses.

3.1.2.1 Realization issues. A simple prototype for the 16-channel version of the MAPMT was recently built by assembling thin aluminum sheets [14]. In this device one has to include the inefficiency produced by the thin sheets making the walls, which does not exist in the total internal reflection tapered light pipes system. Extrapolating the parameters of the prototype based on this design to the 8×8 version one immediately gets a loss of 28%, which might be possibly improved by using thinner sheets.

Another possibility might be to build the device by moulding, followed by an appropriate coating of the internal faces.

Recently a prototype for the 64-channel version was realized by the RIKEN group by means of a laser polymerization technique [11].

3.2 Hemispherical Lenses (HL)

Another option to recover the geometrical acceptance of the MAPMT is by using lenses in front of it. Systems based on lenses have been already described in the literature [15,2,16].

One possible system consists of a plano-convex hemi-spherical lens located in front of the MAPMT with the curved face of the lens facing the incident rays and the plane face in optical contact with the MAPMT input window and coincident with the original focal surface. Alternatively a small gap between the plane face of the lens and the entrance window of the MAPMT might be left, in case the optical coupling between the lens and the MAPMT turns out to be difficult to realize from the engineering point of view. A similar system was recently designed and tested by the RICH-LHCb Collaboration at CERN [15,16,17].

In the paraxial approximation a hemi-spherical lens with the plane face placed on the focal plane of some objective will re-focus the incident rays on the same focal plane but with the image demagnified by a factor given by the refractive index of the lens material. A system of this kind is sometimes known in the literature as an *immersion lens* [8]. Assuming a refractive index $n = 1.5$ the required $\simeq 0.67$ demagnification is obtained.

The radius of curvature of the lens is a free parameter to be optimized as a compromise between the need to limit aberrations (significant for a small curvature radius) and the need to reduce absorption losses inside the lens (significant for a large curvature radius). A baseline radius of the lens of $\approx$ 20 mm is assumed. The lens will be have a square section with a 27 mm side. The minimum lens thickness, at the four corners, is given by the relation $t_{min} = \sqrt{R^2 - l^2/2}$ as a function of the lens radius, R, and lens side l. For the radius $R = 20$ mm one has $t_{min} = 6.0$ mm. The minimum possible lens radius is given by $R = \sqrt{l^2/2}$.

A view of the lens with some ray tracing, demonstrating the demagnification capabilities of the lens for different field angles, is shown in figure 2, for illustrative purposes.

Aberrations, geometrical as well as chromatic, are important but not critical, because of the low spatial resolution required (of the order of a few mm).

The system is very attractive because it is very simple and cheap. It has however some limits whose effects have to be carefully examined. The inherent distortions of the image due to aberrations, however small, will make the space resolution worse. A fraction of photons will be reflected at the lens surface, instead of being refracted, with the additional possibility to be collected by another lens and increase the background light. The fact that a photon can reach the lens surface at any angle with the normal, might limit the usefulness of an anti-reflection coating, which should be a broadband and broad-angle one. The spatial resolution might become worse if chromatic aberration would not be negligible.

A major problem is given by the shadowing effect of one lens to its neighboring lenses for rays that fall close to the border between two lenses. In this case one ray might intercept the wrong lens. In fact the ray might intercept not the lens lying on the MAPMT covering the focal surface region toward which the photon would be directed in case the lens is not present, but it might intercept one of nearby lenses. Therefore the photon would be focused and reconstructed onto the wrong region of the focal surface, introducing a degradation of the spatial resolution.

A view of the lens on the MAPMT is shown in figure 3 and a view of an array of MAPMT plus lenses are shown in figure 4.

3.2.1 Prototypes and tests

Prototypes have been built either using the Sol-Gel technology (see section 5) and as classic quartz lenses. The Sol-Gel lenses are under test to ensure they satisfy the requirements, in particular concerning the bulk transmission, mechanical precision and surface finish. The classic quartz lenses have been used in the readout of a cluster of 9 MAPMT to detect Cherenkov light in a test-beam setup by the RICH-LHCb Collaboration at CERN [17].

3.3 Fiber optics tapers

Fiber optic tapers might be used to demagnify the image from the focal surface onto the MAPMT sensitive area. The main limits of commercial fiber optic tapers is that the filling factor of the entrance face (sensitive to total area ratio) is normally of the order of 0.75 [18]. Moreover they are often made of materials that are not suitable for UV applications.

4 Simulations

Detailed simulations of the performance of the different LCS have been carried on, with realistic boundary conditions, in order to evaluate and compare their performance. In all the cases the dependence of the results on properties deriving from general laws is kept separated from the dependence on the properties deriving from the choice of the materials (which are normally wavelength dependent). The only (unavoidable) exception is the refractive index of the transparent materials, which has been set equal to that of quartz in all the cases.

The simulations were carried on having in mind the 64-channel version of the MAPMT, because the design is more challenging, due the large number of channels. A plane bi-dimensional array of MAPMTs was assumed, with a pitch of 27.0 mm between MAPMTs, slightly larger than the real MAPMT side to account for a realistic close packing of the MAPMTs. The effects of the 0.8 mm MAPMT input window, introducing some cross-talk especially for large photon incidence angles, was fully simulated. The average detection efficiency for photons falling in the inter-pixel regions of the MAPMT photocathode is assumed to be a factor two lower than the maximum detection efficiency in the central region of the pixel. This assumption implies, by itself, a loss of collection efficiency of $\simeq 0.11$, inside the nominal $18.4 \times 18.4\ \mathrm{mm}^2$ sensitive area. The reflection losses at the interfaces were fully simulated but, in principle, they might be reduced, in a real design, by a suitable anti-reflection coating.

The results reported in the present paper concern the simulation of a bunch of photons directed onto a bi-dimensional array of MAPMTs, with a uniform distribution in the position of the impact point on the MAPMT plane array, an average incidence direction normal to the MAPMT plane array and a uniform distribution in solid angle. Different bunches were simulated, with different values of θ_{M}: 15°, 20° and 25°. The photons are unpolarized and their wavelength is assumed to be 350 nm, as the interest in all the cases that motivated these studies is for photo-detection in the near-UV wavelength region. All rays are traced until their relative intensity falls below 0.03, which can then be assumed as the overall systematic error of the quoted results.

As a reference figure one should keep in mind that an array of MAPMT, with a 27 mm pitch, would provide, without any LCS, an overall geometrical acceptance of about 0.4.

A general ray tracing code for the photon transport was specifically developed to carry on the simulations.

The optimization of the design of the LCS cannot be done in general terms but require a precise knowledge of the incoming photon distribution. Therefore the results presented in this section should be regarded as an indication of the possible behavior of the LCS.

4.1 Results of the simulations: LP

In the LP simulations the exit face of each pipe is assumed to have a 1.8 mm side, slightly shorter than the pixel size, to avoid the lower efficiency regions at the edges of the pixel and thus reducing the light losses. In fact some photons miss the sensitive MAPMT area, especially for large incidence angles, because the photo-cathode is necessarily located at some distance from the LP exit face. The backside of the LCS is separated, by a 0.2 mm empty gap from the MAPMT input window. This might be a conservative choice as the LCS might be possibly glued to the MAPMT input window.

Roughly speaking photons can be lost either because they bounce back the pipe or they fall onto a low efficiency region of the MAPMT input window. Moreover the light intensity can be attenuated by bulk absorption, reflection losses and total internal reflection violation (for LP-TIR), and by reflection losses on the walls (for LP-R).

4.1.1 Results of the simulations: LP-TIR

It is assumed that two thin plates, 0.5 mm thick, are placed onto the input and exit faces of the LCS to mechanically assemble the pipes, without introducing any light attenuation at the interface between the pipes and the plates.

The present simulations assume that photons violating the total internal reflection condition somewhere inside any pipe, and thus leaking into the space among the pipes, are absorbed before reaching any other pipe. If this is not the case they might produce cross talk in the neighboring pipes.

The light collection efficiency for different lengths of the pipes and for bundles with different θ_{M} is summarized in table 1.

	Length of the pipes (mm)								
	5	**7**	**10**	**15**	**20**	**25**	**30**	**35**	**40**
$\theta_{\mathrm{M}} = \mathbf{15}^\circ$	0.21	0.33	0.51	0.64	0.77	0.79	0.82	0.83	0.84
$\theta_{\mathrm{M}} = \mathbf{20}^\circ$	0.21	0.32	0.47	0.60	0.71	0.76	0.78	0.79	0.80
$\theta_{\mathrm{M}} = \mathbf{25}^\circ$	0.20	0.32	0.45	0.57	0.66	0.69	0.72	0.74	0.75

Table 1
Overall light transport efficiency from the simulation of the LP-TIR system for different lengths of the pipes and for bundles with different θ_{M}. The bulk absorption inside the pipe material is not included. The statistical error from the finite simulated sample amount to 0.02 for all the numbers in the table. The systematic error, as discussed in the text, is 0.03.

The results are also shown in figure 5 where the first plot shows the fraction of photons reaching the photo-cathode (possibly attenuated in their intensity); the second plot shows the average intensity of the photons reaching the photo-cathode; the third plot shows the overall transmission efficiency, a combination of the two previous data. While the only fully meaningful result is the one shown in the third plot, the first two plots roughly split the attenuation between the purely geometrical one, due to the light pipe geometry, (the first plot) and the attenuation due to all the other factors (the second one). The former includes the losses due to photons bouncing back, photons undergoing total internal reflection at the pipe exit face and the losses due to photons falling onto the low efficiency inter-pixel region on the MAPMT. For large LP-TIR length this fraction tends to ≈ 0.9, dominated by the losses inside the low efficiency inter-pixel regions. The latter includes the attenuation from refraction at the input and exit faces of the light pipe and at the MAPMT input window and the attenuation due to normal, instead of total internal, reflection at the walls. For large LP-TIR length this value tends to ≈ 0.9, due to the reflection losses at the three refractive surfaces. One should note that photons might undergo total internal reflection at the exit face, which is particularly significant for short LP. This might be reduced by optically coupling the LCS to the MAPMT input window.

The bulk absorption inside the pipe material is not included. It can be easily roughly estimated, once the material has been chosen, by just taking into account the pipe geometry.

The results take into account all the losses (assuming conservatively no anti-reflection coating), but those coming from the bulk absorption, which depends on the material.

4.1.1.1 Conclusions The results show that an overall efficiency up to ≈ 0.7 can be reached with a 20 mm long pipe, for the bunch of photons with $\theta_{\mathrm{M}} = 20°$, as long as bulk absorption is negligible. Increasing the LP-TIR length helps to improve the photon transport efficiency if and only if bulk absorption is negligible. However increasing the LP-TIR length to more than ≈ 25 mm is of little help.

4.1.2 Results of the simulations: LP-R

A reflecting tapered light pipe system has been simulated. To avoid using any specific model for the reflectivity of the pipes the simulations were carried on assuming a constant reflectivity on the walls, independent of the incidence angle and wavelength, with four different average values: 1.00, 0.96, 0.92 and 0.88. The results, together with the distribution of the incidence angles on the walls and number of reflections, allow to estimate the light losses for any given model of the reflectivity of a specific coating of the walls.

The light collection efficiency for different lengths of the pipes, for bundles with different θ_{M} and for the four chosen average reflectivity of the walls is summarized in table 2. The results are also shown in figure 6 where the overall light transport efficiency is plotted, as a function of the length of the pipes, average reflectivity of the walls and for the three different bundles with different values of θ_{M}: 15°, 20° and 25°.

In a realistic engineering design additional losses have to be included, probably, due to the finite thickness of the reflecting walls, which implies some loss in the geometrical acceptance at the entrance face, as discussed in 3.

The distribution of the incidence angles of the photons on the walls of the pipes is shown in figure 7. The plot refers to a 15 mm length LP-R, corresponding to the length which approximately maximizes the photon transport efficiency of the LP-R, as shown in figure 6.

	Length of the pipes (mm)									
	5	**7**	**10**	**15**	**20**	**25**	**30**	**35**	**40**	**$\bar{\mathrm{R}}$**
	0.32	0.45	0.56	0.60	0.59	0.56	0.54	0.50	0.47	**0.88**
$\theta_{\mathrm{M}} = \mathbf{15}°$	0.35	0.51	0.63	0.68	0.68	0.66	0.64	0.61	0.59	**0.92**
	0.38	0.56	0.71	0.77	0.78	0.76	0.76	0.75	0.73	**0.96**
	0.46	0.68	0.86	0.93	0.94	0.95	0.95	0.95	0.95	**1.00**
	0.31	0.42	0.51	0.55	0.53	0.49	0.45	0.42	0.38	**0.88**
$\theta_{\mathrm{M}} = \mathbf{20}°$	0.34	0.47	0.57	0.63	0.62	0.60	0.57	0.54	0.50	**0.92**
	0.37	0.52	0.65	0.73	0.74	0.73	0.71	0.69	0.67	**0.96**
	0.44	0.63	0.78	0.89	0.92	0.93	0.93	0.93	0.93	**1.00**
	0.31	0.40	0.46	0.48	0.45	0.42	0.38	0.34	0.31	**0.88**
$\theta_{\mathrm{M}} = \mathbf{25}°$	0.34	0.44	0.52	0.56	0.55	0.52	0.49	0.46	0.43	**0.92**
	0.37	0.49	0.59	0.66	0.67	0.66	0.65	0.63	0.60	**0.96**
	0.44	0.59	0.71	0.82	0.87	0.90	0.91	0.91	0.92	**1.00**

Table 2
Overall light transport efficiency from the simulation of the LP-R system for different lengths of the pipes and for bundles with different θ_{M} and for different average reflection coefficient of the walls. For each bundle the results for four different values of the average reflection coefficient of the walls (1.00, 0.96, 0.92 and 0.88) are shown. The statistical error from the finite simulated sample amount to 0.02 for all the numbers in the table. The systematic error, as discussed in the text, is 0.03.

The distribution of the number of reflections the photons undergo on the walls of the pipes is shown in figure 8, for a 15 mm long LP-R.

4.1.2.1 Conclusions The results show that, except for the case of negligible reflection losses at the walls, the optimum LP-R length is 15 mm$\div$20 mm. Increasing the LP-R length helps to improve the photon transport efficiency if and only if the reflection losses at the walls are negligible. However increasing the LP-R length to more than $\approx$ 25 mm is of little help. The overall photon transport efficiency strongly depends on the walls reflectivity and quickly decreases as the average wall reflectivity drops.

4.2 Results of the simulations: HL

An array of lenses with square section, side l = 26.8 mm, a pitch between MAPMT/lenses of Δ = 27.0 mm and a 0.2 mm total absorption layer between the lenses was simulated, with different radii of curvature (20 mm, 22 mm, 24 mm and 26 mm). The full simulation of the bi-dimensional array was carried on, taking into account cross-talk between neighboring MAPMTs/lenses.

Absorption inside the lens material is ignored because it depends on the specific material and it only contributes as an overall multiplicative factor that can be estimated once the path lengths inside the material are known. The average path length inside the lens is roughly equal to the lens radius.

An empty gap of 0.2 mm was assumed between the lens and the MAPMT input window, to be conservative in case an optical coupling between the lens and the MAPMT input window is not technically feasible.

The results of the simulation are summarized in table 3. These results apply to the 64-channel version of the MAPMT. In the case of the 16-channel the distortions are much less relevant due to the larger pixel size. One should note that the lens can do nothing to avoid the low efficiency inter-pixel regions, in sharp contrast with the LP systems.

	Lens radius (mm)			
	20	22	24	26
$\theta_{\mathrm{M}} = \mathbf{15}^\circ$	0.70	0.69	0.68	0.66
$\theta_{\mathrm{M}} = \mathbf{20}^\circ$	0.68	0.66	0.65	0.63
$\theta_{\mathrm{M}} = \mathbf{25}^\circ$	0.66	0.63	0.61	0.58

Table 3
Results of the simulation of the light collection efficiency of the HL system as a function of the lens radius and the θ_{M}. All the losses are included except for the bulk absorption, material dependent. The statistical error from the finite simulated sample amount to 0.02 for all the numbers in the figure. The systematic error, as discussed in the text, is 0.03.

The results take into account all the losses (assuming conservatively no anti-reflection coatings), the inefficient inter-pixel region but ignore the bulk absorption, which depends on the material. Note that, if there is no optical coupling between LCS and MAPMT, total internal reflection can occur on the back face of the lens. This is most likely to occur close to the four corners of the lens.

The reflection losses at the interfaces, the two lenses surfaces plus the MAPMT input window, are, in all the cases, 0.11 ± 0.05. The distribution of the transmitted light intensity by the three surfaces, for a lens radius of $r = 24$ mm, is shown in figure 9.

The assumptions about the inter-pixel losses (see section 2), included in the quoted results, imply, by itself, a loss of collection efficiency of $\simeq 0.11$.

As in the case of LP-TIR the bulk absorption inside the lens material is not included. It can be easily roughly estimated, once the material has been chosen, by just taking into account the lens geometry.

The lens introduces a degradation of the spatial resolution corresponding to about one pixel (for the 64-channel MAPMT) for less than one third of the reconstructed rays. The effect would be much smaller for the 16-channel type, due to the larger pixels. While the degradation of the spatial resolution is about constant while changing radius and the θ_{M}, the overall acceptance degrades quickly increasing the lens radius or the θ_{M}.

The effect of a naive reconstruction algorithm, assuming a perfect demagnification of 3 : 2 by the HL, is shown in figure 10: photons directed towards a single MAPMT region are reconstructed as shown in figure, for $\theta_{\mathrm{M}} = 20°$ and a lens radius of 24 mm. The plot clearly shows the one pixel spatial resolution degradation, which is stronger at the edges of the lenses.

The effect of chromatic aberration on the spatial resolution, which is material dependent, has not been considered.

A more refined lens design can help to recover the photons lost because they miss the sensitive area of the neighboring MAPMTs, possibly at the price of a decrease of the space resolution. A preliminary study shows that a biconvex lens as well as aspherical surfaces can improve in a substantial way the performance.

4.2.0.2 Conclusions The results show that an overall efficiency up to ≈ 0.7 can be reached with the HL, depending on θ_{M}, with about two-thirds of the photons reconstructed in the correct pixel and the others in one of the nearby pixels. Absorption inside the lens material has been neglected, but this is a reasonable assumption for many materials, at least in visible light.

5 Environmental and engineering issues

5.1 Optical coupling to the MAPMT input window

The optical coupling between the LCS and the MAPMT input window is not a trivial matter due to the rather large deviation from planarity of the MAPMT input window compared to the light wavelength. As the Hamamatsu technical specifications do not provide details about the flatness of the MAPMT input window, nor about the parallelism between the input window and any reference surface on the MAPMT itself, some measurements were made on some MAPMTs [16]. The measurements were performed on two MAPMTs with borosilicate window and one MAPMT with UV-extended borosilicate window. After scanning the MAPMT window with a step of about 2 mm in two directions roughly parallel to the MAPMT sides, the data were fitted to a plane. The maximum distance, in the direction perpendicular to the fitted plane, between any two points was found to be 0.02 mm, for the MAPMT with UV-extended borosilicate window, and 0.03 mm for the two MAPMTs with borosilicate window.

5.2 Choice of the materials

The performance of any LCS is strongly dependent on the availability of materials with suitable optical properties. In fact a successful reconstruction of the events requires that the light losses are kept to the minimum. Absorption inside the LCS can be easily estimated, after the material has been chosen, from the data of section 4.

5.2.1 LP-R

An UV-enhanced aluminum coating would provide a reflectivity of ≈ 0.9 at normal incidence in the near UV. Assuming, very roughly, this figure as an estimate for the average reflection coefficient one can see that five reflections already provide an overall attenuation of about 0.4 (compare with figure 8).

A coating based on dielectric layers would require a very high reflectivity in a large range of angles, up to grazing incidence in the full wavelength band of interest.

5.2.2 HL and LP-TIR.

The two systems share the same requirements concerning the choice of the materials. The choice of the material is strongly driven by the required operating wavelength range.

The use of PMMA or other plastics might be the best choice for visible light.

The choice is less trivial for near-UV applications. Quartz would not give any problem for the transmission but the mass of the LCS would then be comparable to the MAPMT mass. The Sol-Gel silica technology [19,20], allowing to produce high purity silica optics by means of a molding process, is an interesting choice when a large number of devices is required, also because the use of MAPMTs with ≈ 2 mm pixel size implies that a high quality optics is not required.

Polymers have become recently available having good physical qualities, see [4].

5.3 Impact of the light collector on the photo-detector

In case the LCS has to operate in an environment with a significant background from high-energy charged particles, the impact of the production of Cherenkov and scintillation light by fast particles passing through the LCS has to be accounted for. In any case a high-energy particle crossing the LCS would produce a background signal of very short time duration (a few tens of ns) which would be easily distinguishable from other signals in most applications.

Mass might be an important issue in many applications. The total internal reflection light pipe collector and the hemi-spherical lens collector, assuming they are made of quartz, have a mass roughly similar to the mass of the MAPMT alone while the mass is about halved if they are made of plastics. The reflecting light pipes system would have in any case a considerably lower mass.

In cases where electric and/or magnetic screens need to be used the simple hemispherical lens might be not suitable because of the necessity for the screen to extend somewhat beyond the MAPMT input window. This might effectively act as a field stop, cutting the field of view.

6 Comparison

A schematic comparison of the main properties of the LCS discussed are summarized in table 4.

	HL	LP-TIR	LP-R
mass	high, mat. dep.	high, mat. dep.	small
internal transmission	mat. dep.	mat. dep.	mat. dep.
PSF degradation	yes	small	small
recovery of the inter-pixel region	no	yes	yes
engineering	easy	difficult	difficult
cost	cheap	to be defined	to be defined

Table 4
A schematic comparison of the characteristics of the different LCS.

When mass is not a concern and recovering a rather uniform geometrical acceptance on the focal surface is an important item the hemi-spherical lens is a good solution.

When working in visible light PMMA is a good choice for the material. If mass is not a concern quartz, either in the classical and in the Sol-Gel molded version, allows good transparency in the near-UV also.

7 Conclusions

The performance of different LCS, recently proposed to recover the geometrical acceptance of commercial MAPMTs, has been evaluated.

The estimates of their performance is based on realistic assumptions, and it was carried on for different designs and operating conditions (e.g. the $f/\#$ of the primary optics).

Emphasis was put on the study of realistic designs, keeping in mind engineering issues.

The detailed design of any LCS, its optimisation and the resulting performance, will depend on the details of the specific situation. The results presented can be assumed as guidelines provided by a test-case study.

8 Acknowledgements

The author wishes to thank V. Gracco (University of Genova), P. Mazzinghi (INOA, Firenze), O. Catalano (IASF-CNR, Palermo), R. Forty (CERN) and H. Shimizu (RIKEN) for many useful discussions. S. Cuneo and M. Ameri (INFN, Genova) produced some of the drawings.

References

[1] B. Alpat, Nucl. Phys. B Proc. Suppl., 85, (2000) 15.

[2] D. R. Broemmelsiek, Nucl. Instr. and Meth. A, 433 (1999) 136.

[3] S. A. Wotton, Nucl. Instr. and Meth. A, 453 (2000) 296.

[4] O. Catalano, *AirWatch from Space*, Progress Report, IFCAI-CNR Internal Note, 24/09/1999;

M. Ambriola et al., The AirWatch Collaboration, Nucl. Phys. Proc. Suppl., 70 (1999) 515-517;
L. Scarsi et al., EUSO Collaboration, *EUSO - Extreme Universe Space Observatory*, Proposal for the ESA F2/F3 Mission, January 2000.

[5] Multi-anode Photo-Multiplier tube R7600, Hamamatsu Photonics K. K..

[6] Hamamatsu Photonics K. K..

[7] T. Jannson and R. Winston, J. Opt. Soc. Am. A, Vol. 3, No. 1, (1986) 7;
R. Winston and W. T. Welford, J. Opt. Soc. Am. A, Vol. 4, No. 3, (1987) 545.

[8] W. J. Smith, *Modern optical engineering*, McGraw-Hill, 1966;
R. W. Ditchburn, *Light*, Academic Press, 1976.

[9] V. Gracco and A. Petrolini, *Use of multi-anode Photo-Multipliers for the AirWatch photon detector*, 23 October 1998, AirWatch technical note, available at `http://www.ge.infn.it/euso/docs/mapmt.ps`.

[10] V. Gracco and A. Petrolini, *Study of a possible light collector system for multi-anode Photo-Multiplier tubes*, LHCb-RICH note, LHCb 1999-005, CERN, 15/12/1998.

[11] H. Shimizu, RIKEN, private communication.

[12] Precision Glass Products Company, Oreland, PA, USA.

[13] J. Pouxe, ISN Grenoble, private communication.

[14] K. Arisaka, UCLA, private communication.

[15] R. Forty, *Use of lenses to increase the RICH photo-detector coverage*, LHCb-RICH note 1998-038, CERN, 20/03/1998.

[16] S. Cuneo et al., *A proposal for a supporting structure for the multi-anode Photo-Multipliers of RICH2*, LHCb-RICH note 2000-005, CERN, 19/02/2000.

[17] V. Gibson, A. Petrolini et al., *Performance of a cluster of Multi-Anode Photo-Multipliers equipped with lenses for use in a prototype RICH detector*, LHCb-RICH note 2000-083, CERN, 04/07/2001, accepted for publication on Nucl. Instr. and Meth. A.

[18] Schott Fiber Optics Inc., Southbridge, MA, USA.

[19] Laser Focus World, 12/95.

[20] GDE s.r.l., via Faurer 4, Novara, I-28100, Italy;
Geltech Inc., Orlando, Florida, USA.

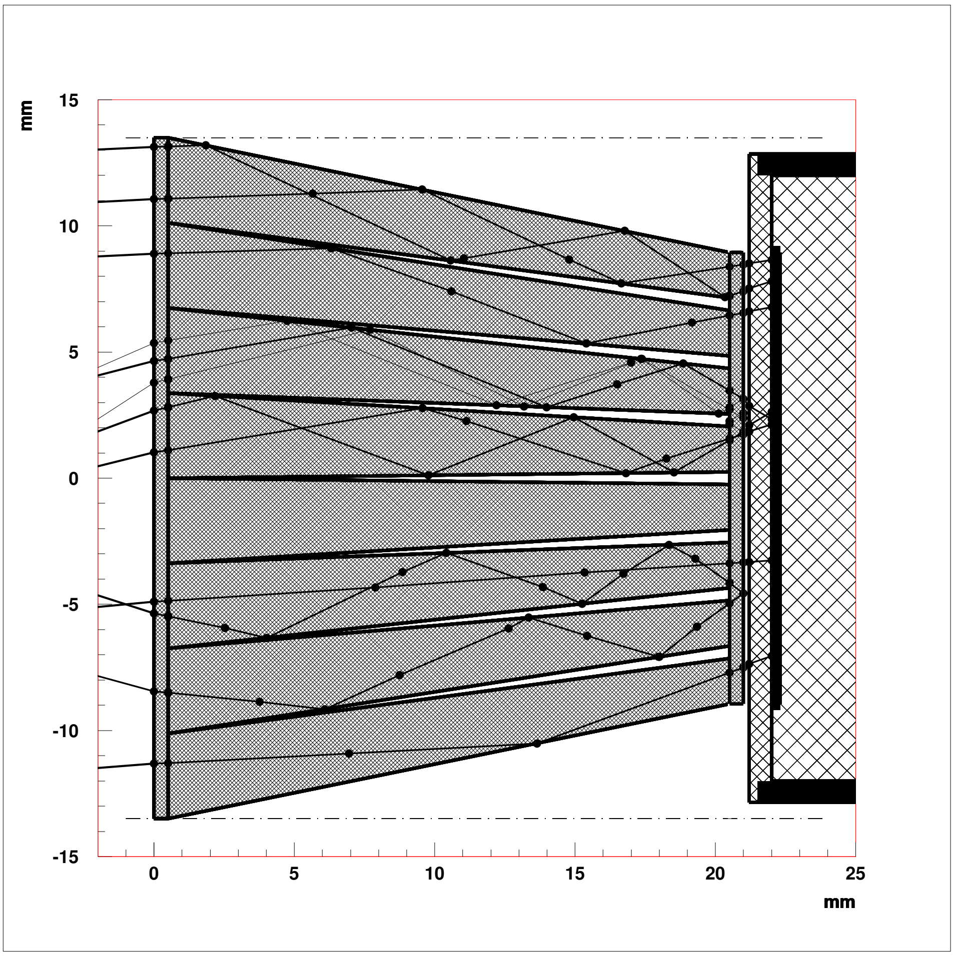

Figure 1. Example of the tracing of ten rays inside a LP-TIR. The line thickness approximately simulates the relative ray intensity and dots represent points where the rays meet the interface between two surfaces. The length of the pipes is 20 mm. Two 0.5 mm thick input and exit plates are also simulated. The structure on the right of the figure represent schematically the MAPMT, with the photo-cathode (black) and the MAPMT 0.8 mm thick input window (dark-hatched) and the MAPMT case (light-hatched). Units are mm.

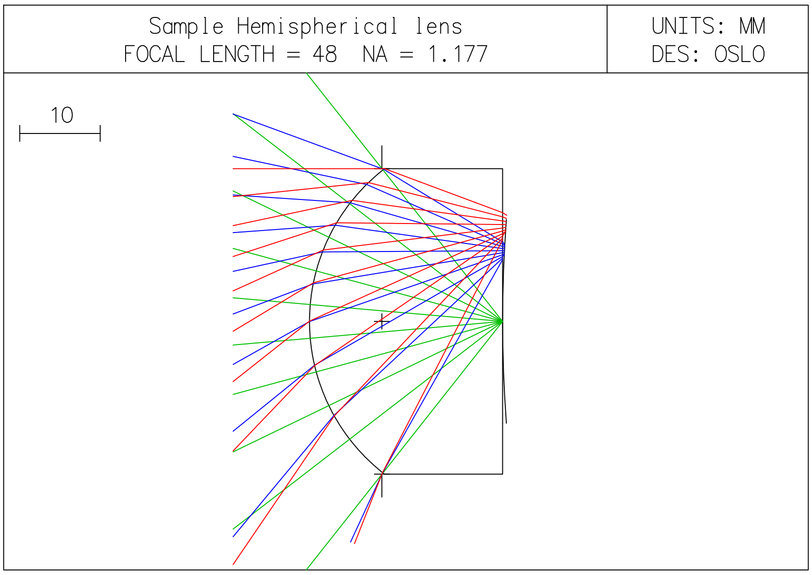

Figure 2. Illustrative example of ray tracing through the hemi-spherical lens (simulated with Oslo 6.04 from Sinclair Optics, Inc.). The ray tracing clearly shows the demagnification capability of the lens.

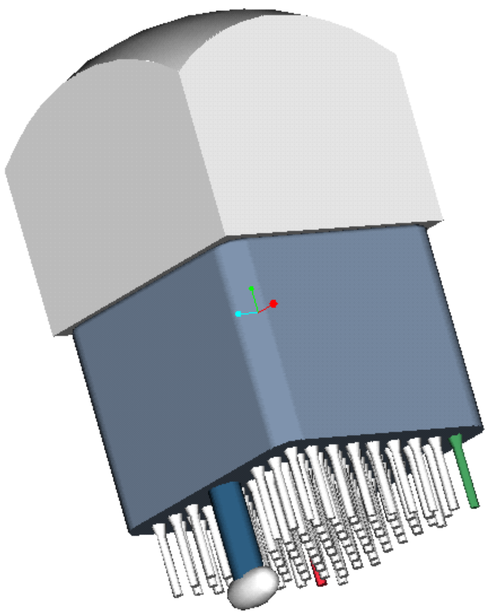

Figure 3. The hemi-spherical lens mounted onto the MAPMT.

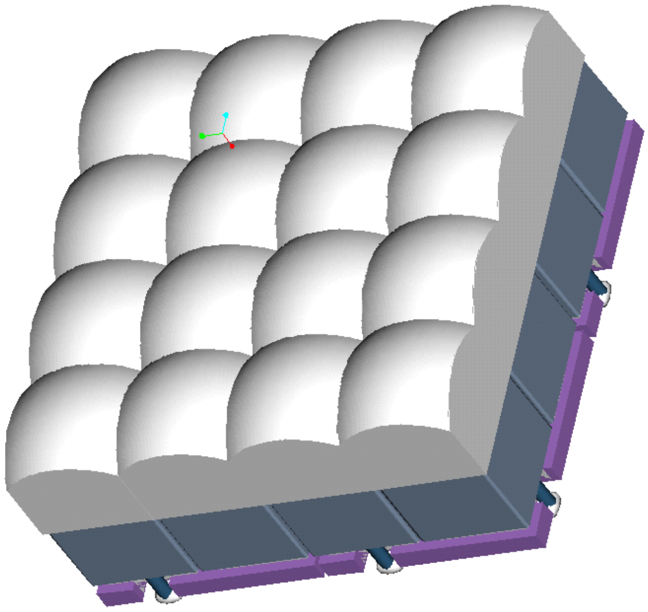

Figure 4. The array of MAPMT plus hemi-spherical lenses.

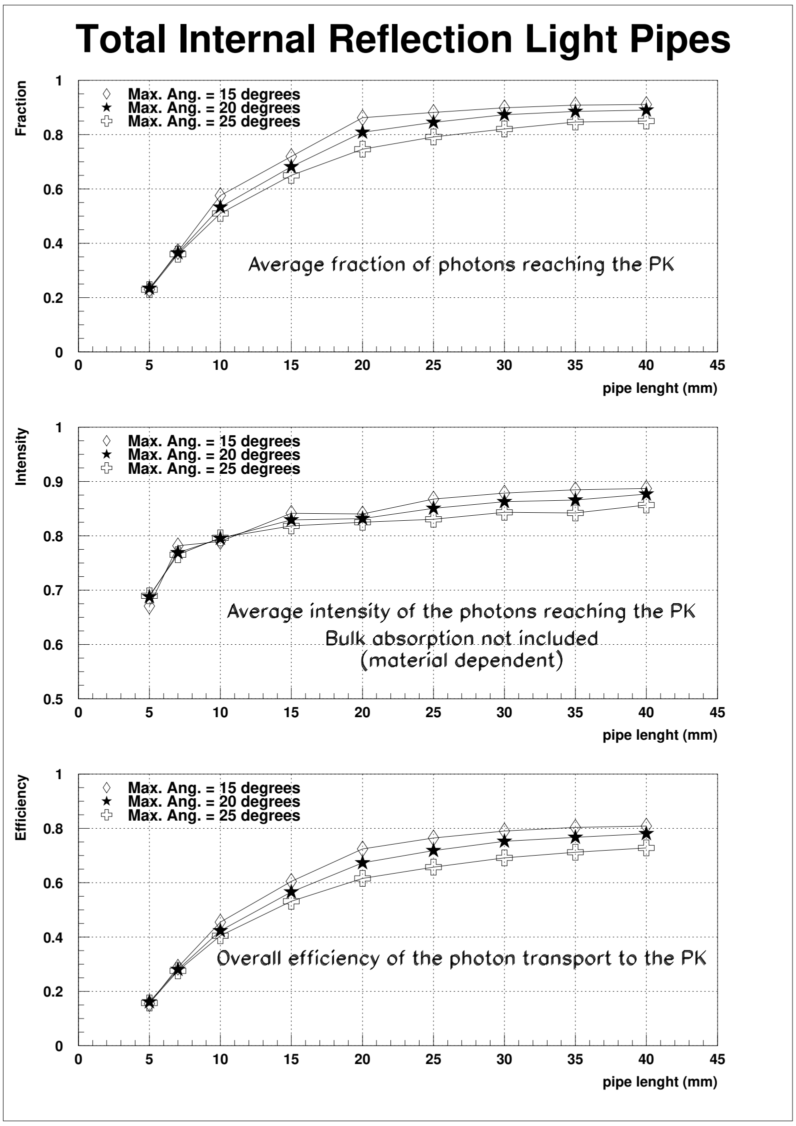

Figure 5. Results of the simulation of the light collection efficiency of the LP-TIR system for different lengths of the pipes and for bundles with different θ_{M}. The bulk absorption inside the pipe material is not included. The statistical error from the finite simulated sample amount to 0.02 for all the numbers in the figure. The systematic error, as discussed in the text, is 0.03.

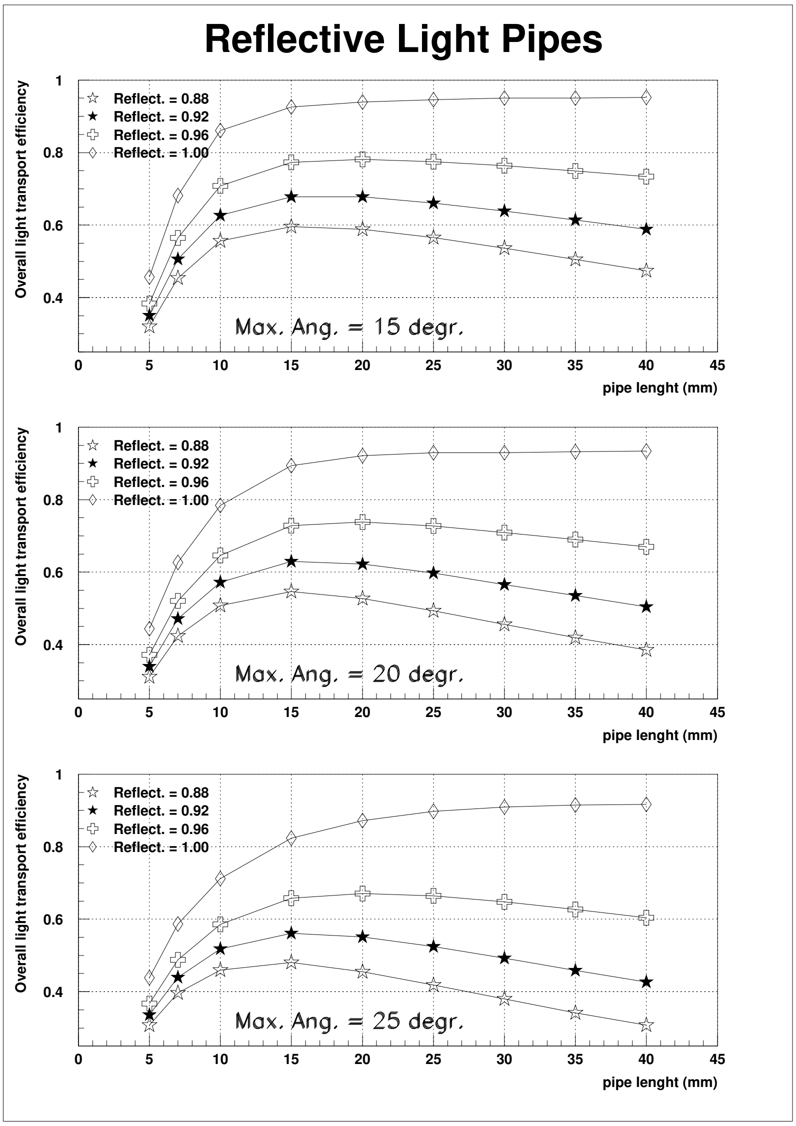

Figure 6. Results of the simulation of the overall light collection efficiency of the LP-R system for different lengths of the pipes and for bundles with different θ_{M} and for different average reflection coefficient of the walls. For each bundle the results for four different values of the average reflection coefficient of the walls (1.00, 0.96, 0.92 and 0.88) are shown. The statistical error from the finite simulated sample amount to 0.02 for all the numbers in the figure. The systematic error, as discussed in the text, is 0.03.

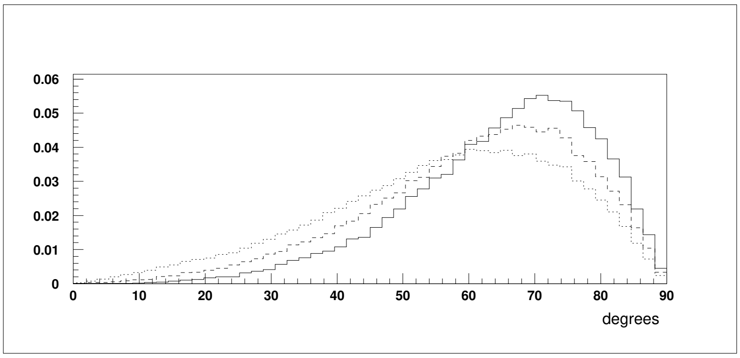

Figure 7. Distribution of the incidence angles (in degrees) with respect to the normal to the walls in the 15 mm long LP-R, for the three bundles of photons with $\theta_{\mathrm{M}} = 15°$ (continuous line), $\theta_{\mathrm{M}} = 20°$ (dashed line) and $\theta_{\mathrm{M}} = 25°$ (dotted line).

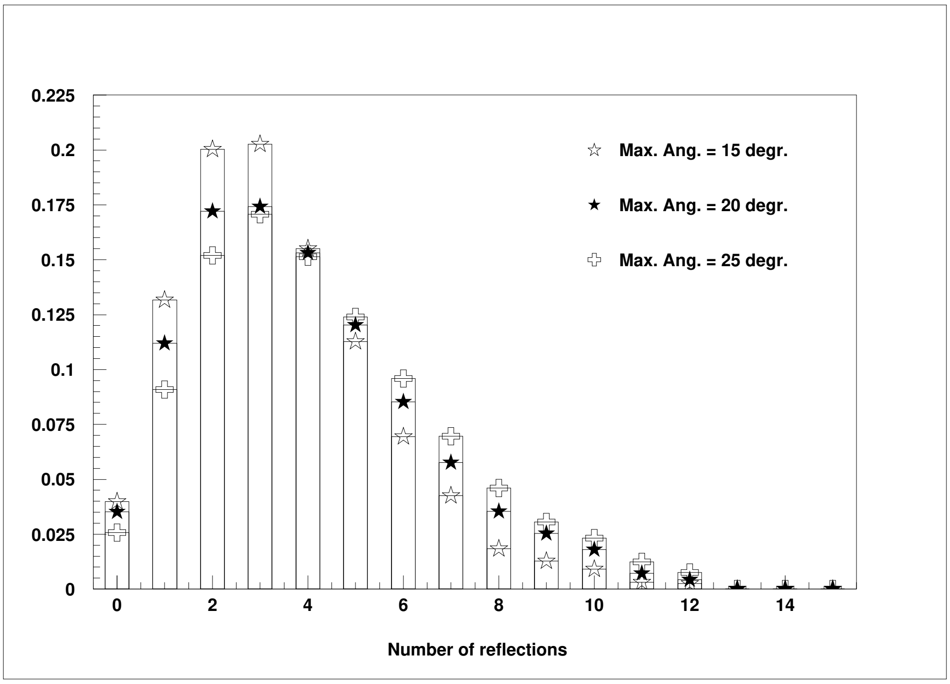

Figure 8. Number of reflections of the photons on the walls of the LP-R for a 15 mm long LP-R and for the three bundles of photons with $\theta_{\mathrm{M}} = 15°$, $\theta_{\mathrm{M}} = 20°$ and $\theta_{\mathrm{M}} = 25°$. The analogous distribution for the LP-TIR system is essentially the same, the only difference in the ray-tracing being the first refraction at the LP-TIR entrance.

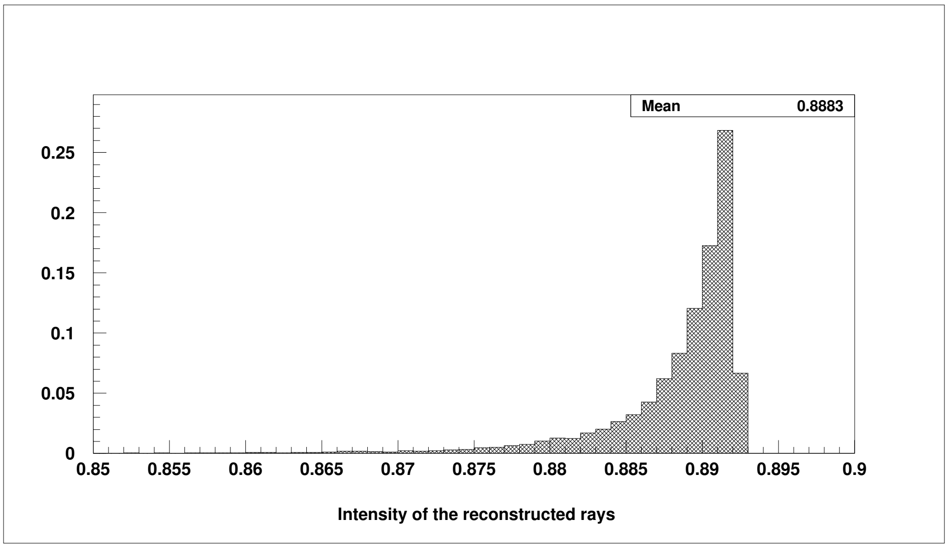

Figure 9. Distribution of the overall transmitted light intensity by the three refracting surfaces of the HL (the two lens surfaces plus the MAPMT input window). The lens radius is $r = 24$ mm and photons have $\theta_{\mathrm{M}} = 20°$. The results are largely independent on the lens radius and θ_{M}.

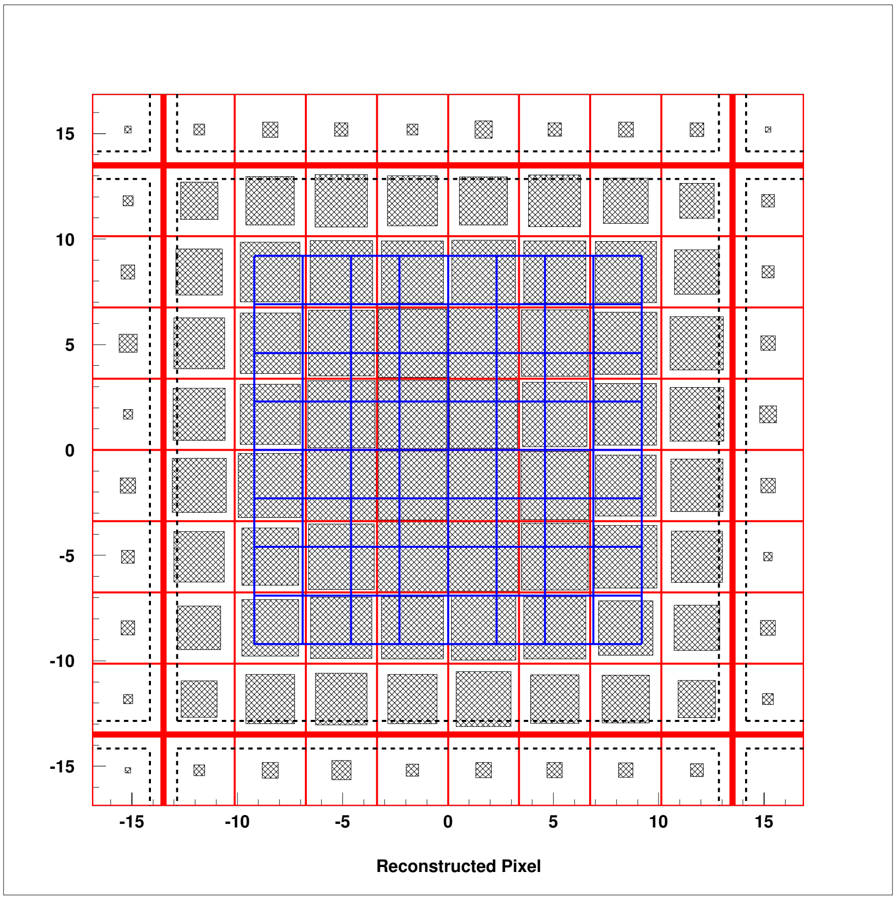

Figure 10. Results of a naive reconstruction algorithm for the HL system, assuming a perfect demagnification of 2/3. In the figure the thick continuous lines represent the 27 mm pitch grid between the MAPMTs; the dashed lines represent the real MAPMT contours; the big squares, partitioning the 27×27 mm^2 area on the focal surface into 8×8 effective pixels, represent the ideal pixels on the focal surface; the smaller square matrix at the center (25.7×25.7 mm^2) represents the real MAPMT sensitive pixels. Photons directed towards a single MAPMT region (the 27×27 mm^2 region at the center of the figure), for $\theta_{\mathrm{M}} = 20°$ and a lens radius of 24 mm, are reconstructed in the pixel as shown in figure. The dimension of the squares at the center of each pixel are proportional to the number of photons reconstructed in that pixel. The fact that some photons are reconstructed in one of the neighboring MAPMTs is clearly visible.